

Co-Construction of Solid Solution Phase and Void Space in Yolk–Shell $\text{Fe}_{0.4}\text{Co}_{0.6}\text{S}@N$ -Doped Carbon to Enhance Cycling Capacity and Rate Capability for Aluminum-Ion Batteries

Jiening Zheng,[§] Shunlong Ju,[§] Guanglin Xia, Hongge Pan, and Xuebin Yu*

Cite This: <https://doi.org/10.1021/acsami.1c24510>

Read Online

ACCESS |

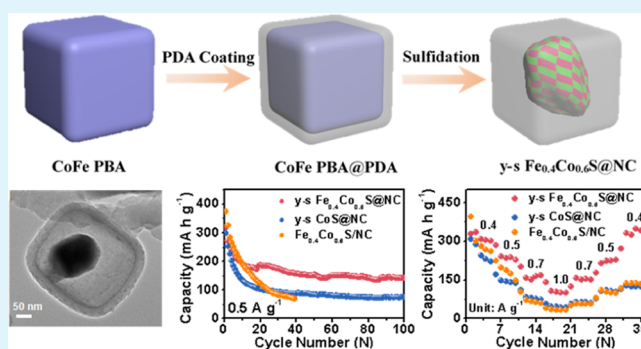
Metrics & More

Article Recommendations

Supporting Information

ABSTRACT: Rechargeable aluminum-ion batteries (AIBs), using low-cost and inherent safety Al metal anodes, are regarded as promising energy storage devices next to lithium-ion batteries. Currently, one of the greatest challenges for AIBs is to explore cathodes suitable for feasible Al^{3+} insertion/extraction with high structure stability. Herein, a facile co-engineering on solid solution phase and cavity structure is developed via Prussian blue analogues by a simple and facile sulfidation strategy. The obtained uniform yolk–shell $\text{Fe}_{0.4}\text{Co}_{0.6}\text{S}@N$ -doped carbon nanocages (γ - $\text{Fe}_{0.4}\text{Co}_{0.6}\text{S}@NC$) display a high reversible capacity of $141.3 \text{ mA h g}^{-1}$ at 500 mA g^{-1} after 100 cycles and a good rate capability of $100.9 \text{ mA h g}^{-1}$ at 1000 mA g^{-1} . The improved performance can be mainly ascribed to the dual merits of the composite; that is, more negative Al^{3+} formation energy and improved Al^{3+} diffusion kinetics favored by the solid solution phase and Al^{3+} insertion/extraction accommodable space stemmed from the yolk–shell structure. Moreover, the reaction mechanism study discloses that the reaction involves the intercalation of Al^{3+} ions into $\text{Fe}_{0.4}\text{Co}_{0.6}\text{S}$ to generate $\text{Al}_x\text{Fe}_m\text{Co}_n\text{S}$ and elemental Fe and Co.

KEYWORDS: solid solution phase, yolk–shell, nitrogen-doped carbon, aluminum-ion battery, diffusion kinetics



1. INTRODUCTION

Energy crisis and environment pollution arising from fossil fuel usage are two global focuses, and thus, exploring environment-friendly energy storage systems with high performance is urgently needed. Currently, lithium-ion batteries (LIBs) are widely used in portable electronic devices as well as electric vehicles because of their high specific energy and power density.^{1–3} Unfortunately, drawbacks such as high cost and safety issues restrict their further development and applications.^{4–7} New types of multivalent ion batteries based on $\text{Mg}^{2+}/\text{Zn}^{2+}/\text{Al}^{3+}$ storage have attracted considerable attention because of their abundance, safety, and high theoretical volumetric energy densities.^{8–11} Among them, aluminum-ion batteries (AIBs) are regarded to be promising candidates because of the rich abundance of aluminum element and high theoretical capacity (gravimetric: 2980 mA h g^{-1} , volumetric: $8063 \text{ mA h cm}^{-3}$).^{12,13} The early category AIBs use graphite materials as cathodes based on AlCl_4^- intercalation and achieve good cycling performance and high power density originating from a high discharge potential and charge/discharge current density.^{14,15} However, their capacities are usually low because of the monovalent AlCl_4^- storage properties.¹⁶ What is more, the large steric hindrance of AlCl_4^- may lead to heavy structural damage of these materials.¹⁷ Alternatively, another category of AIBs with Al^{3+}

ions as the intercalation/conversion reagent have aroused considerable interest. These cathode materials mainly include transition metal oxides, chalcogenides, phosphides, and a few others.^{18–23} In particular, transitional metal chalcogenides, because of their rich source, easy fabrication, and high theoretical capacity, have been studied extensively in AIBs.²⁴ The initial discharge capacity of a majority of these materials can easily reach higher than 200 mA h g^{-1} ; nevertheless, they have critical issues of poor long-term cycling stability leading to the residual capacity of less than 100 mA h g^{-1} after 100 cycles and slow Al^{3+} solid diffusion rate leading to deficient rate performance.^{25–27} In fact, trivalent Al^{3+} has an intrinsically high charge density and typically exhibits strong Coulombic interactions with the host lattices, which leads to severe structural damage and sluggish Al^{3+} diffusion kinetics.²⁵ To some extent, these problems can be managed by fabricating nanomaterials to decrease the diffusion distance, coating or

Received: December 22, 2021

Accepted: January 13, 2022

loading with conductive carbon materials to improve mechanical stability as well as conductivity, and using open-tunnel structures or layered materials with large interlayer distances to facilitate Al^{3+} diffusion.^{16,21,28,29} Although improved electrochemical performances have been achieved, issues such as poor intrinsic ionic conductivity still need to be addressed.

Recently, we have fabricated MXene and nitrogen-doped carbon dual protected $\text{Ni}_{0.6}\text{Co}_{0.4}\text{S}$ nanocomposite, in which density functional theory (DFT) results confirmed that the incorporated Ni could tune the binding interaction of $\text{Ni}_{0.6}\text{Co}_{0.4}\text{S}$ with the Al^{3+} ions and decrease the Al^{3+} ions diffusion barrier.³⁰ Additionally, based on first-principle calculation, Pal et al. found that $\text{Mo}_{1-x}\text{W}_x\text{S}_2$ alloys displayed decreased Li^+ ion diffusion barrier than that of MoS_2 .³¹ Huang et al. reported that the Ni-doped Mn_2O_3 could facilitate the diffusion of $\text{H}^+/\text{Zn}^{2+}$ ions.³² These results suggest that the transition metal doping or alloying could induce electron redistribution, which could improve the ion conductivity, leading to fast ion diffusion in various battery systems.^{30,33}

In addition, constructing nanostructures with specific morphologies is an effective method to further improve their electrochemical performances. Especially, yolk-shell structures have attracted growing research interests in energy storage applications for their outstanding structural properties.^{34,35} First, the core always consists of active materials, which increases the total weight proportion of the active component. Second, the outer protective shell can prevent the nanoparticles from aggregation. More importantly, the hollow space between the yolk and the shell can accommodate the volume expansion and ease the electrode pulverization problem.^{36–38} For example, Liu et al. successfully fabricated yolk-shell structured CuSi_2P_3 @graphene nanocomposite, which displayed excellent lithium-ion storage ability with enhanced long-term cycling stability and rate capability.³⁹ Wang et al. synthesized a yolk-shell CoMoO_xS_y nanosphere via the solid CoMo-glycerate nanospheres. They showed improved sodium-ion storage performance over hollow CoMoO_xS_y nanospheres.⁴⁰ Bao et al. prepared the yolk-shell FeS/MoS_2 @N-doped carbon nanocubes based on a metal-organic framework precursor, which manifested remarkable ultra-long cycling stability for K^+ storage.⁴¹ Nevertheless, the construction of solid solution compounds with the yolk-shell structure for AIBs has been rarely explored.

Herein, $\text{CoS}@C$ yolk-shell nanocages incorporated with Fe atoms ($\gamma\text{-s Fe}_{0.4}\text{Co}_{0.6}\text{S}@NC$) have been rationally designed and employed as the cathode for AIBs. The incorporation of Fe greatly decreases the Al^{3+} ion formation energy as well as improves the Al^{3+} diffusion rate of CoS. In addition, the unique yolk-shell structure where the carbon shell can enhance the conductivity together with protecting $\text{Fe}_{0.4}\text{Co}_{0.6}\text{S}$ from aggregation during preparation and cycle tests and the interior void space can mitigate the volume change as well as promote the electrolyte penetration. As a result, the as-synthesized $\gamma\text{-s Fe}_{0.4}\text{Co}_{0.6}\text{S}@NC$ delivers a high initial discharge capacity of $317.2 \text{ mA h g}^{-1}$, and the reversible discharge capacity can be maintained at $141.3 \text{ mA h g}^{-1}$ at 0.5 A g^{-1} after 100 cycles.

2. EXPERIMENTAL SECTION

2.1. Synthesis of CoFe PBA and CoFe PBA@PDA. First, 1.7462 g of cobaltous nitrate hexahydrate and 2.3226 g of trisodium citrate were added into deionized water (200 mL) to form a uniform solution labeled as A. Then, 1.3170 g of potassium ferricyanide was

dispersed into the same amount of deionized water, which was labeled as solution B. Solution A was then poured into B under continuous stirring for 10 min. Subsequently, the mixture was aged for a day without stirring at ambient room temperature (RT). Finally, the dark violet precipitates were retrieved by centrifugation, washed three times with distilled water and ethanol, and then vacuum-dried at 60°C overnight. The CoFe PBA@PDA was prepared in a similar way as previously reported by us for NiCo PBA@PDA.³⁰ In addition, the CoCo Prussian blue analogues (PBA) and CoCo PBA@PDA were synthesized similarly using $\text{Co}(\text{NO}_3)_2 \cdot 6\text{H}_2\text{O}$ and $\text{K}_3[\text{Co}(\text{CN})_6]$ as starting materials, respectively.

2.2. Synthesis of $\gamma\text{-s Fe}_{0.4}\text{Co}_{0.6}\text{S}@NC$. The $\gamma\text{-s Fe}_{0.4}\text{Co}_{0.6}\text{S}@NC$ was synthesized by a facile sulfidation process in a tubular furnace. Typically, CoFe PBA@PDA and thiourea with a feed ratio of 1:5 were placed in the upstream and downstream side, respectively. The temperature of the tubular furnace was first increased to 500°C at a heating rate of 1°C min^{-1} and held for 3 h under Ar flow. The yolk-shell $\text{Fe}_{0.4}\text{Co}_{0.6}\text{S}@NC$ nanocomposites were obtained after natural cooling of the tubular furnace to RT. For comparison, $\gamma\text{-s CoS}@C$ and $\text{Fe}_{0.4}\text{Co}_{0.6}\text{S}/NC$ were prepared similarly using CoCo PBA@PDA and CoFe PBA as precursors, respectively.

2.3. Material Characterizations. The X-ray diffraction (XRD), transmission electron microscopy (TEM), scanning electron microscopy (SEM), X-ray photoelectron spectroscopy (XPS), thermogravimetric analysis (TGA), inductively coupled plasma-optical emission spectroscopy, and Brunauer–Emmett–Teller specific surface areas were measured similar to our previous reports.^{23,30,42}

2.4. Electrochemical Measurements. The electrochemical measurements were also conducted similar to our previous report.³⁰

2.5. Computational Method. DFT calculations were also similar to our previous report.³⁰

3. RESULTS AND DISCUSSION

The preparation procedure of $\gamma\text{-s Fe}_{0.4}\text{Co}_{0.6}\text{S}@NC$ is schematically illustrated in Figure 1. First, the $\text{Co}_3[\text{Fe}(\text{CN})_6]_2 \cdot n\text{H}_2\text{O}$ (CoFe PBA) precursor was synthesized by the reaction of Co^{2+} cations and $\text{Fe}[(\text{CN})_6]^{3-}$ anions with the aid of sodium citrate. The obtained CoFe PBA precursor has a highly uniform cubic morphology with a smooth surface (Figure 2a). The average size is about 238.6 nm (inset in Figure 2a). Then, the CoFe PBA nanocubes were covered with polydopamine (PDA), forming core-shell CoFe PBA@PDA nanocubes with an average size of $\sim 303 \text{ nm}$ (inset in Figure 2b). Different from the smooth surface of CoFe PBA, the surface of CoFe PBA@PDA becomes rough (Figure 2b). XRD

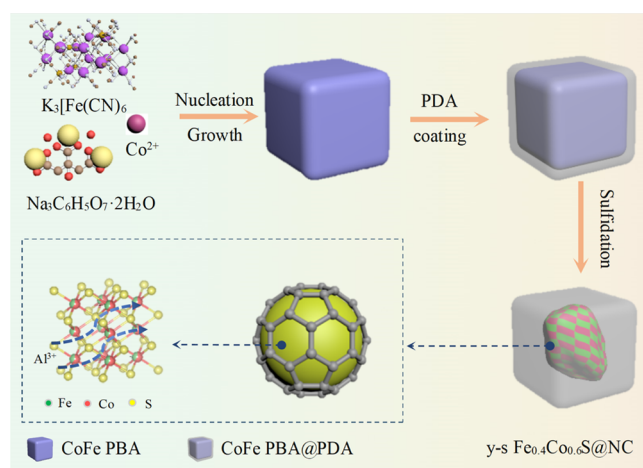


Figure 1. Schematic illustration for the fabrication of the $\text{Fe}_{0.4}\text{Co}_{0.6}\text{S}@NC$ composite.

$(\text{CN})_6]_2 \cdot n\text{H}_2\text{O}$ (CoFe PBA) precursor was synthesized by the reaction of Co^{2+} cations and $\text{Fe}[(\text{CN})_6]^{3-}$ anions with the aid of sodium citrate. The obtained CoFe PBA precursor has a highly uniform cubic morphology with a smooth surface (Figure 2a). The average size is about 238.6 nm (inset in Figure 2a). Then, the CoFe PBA nanocubes were covered with polydopamine (PDA), forming core-shell CoFe PBA@PDA nanocubes with an average size of $\sim 303 \text{ nm}$ (inset in Figure 2b). Different from the smooth surface of CoFe PBA, the surface of CoFe PBA@PDA becomes rough (Figure 2b). XRD

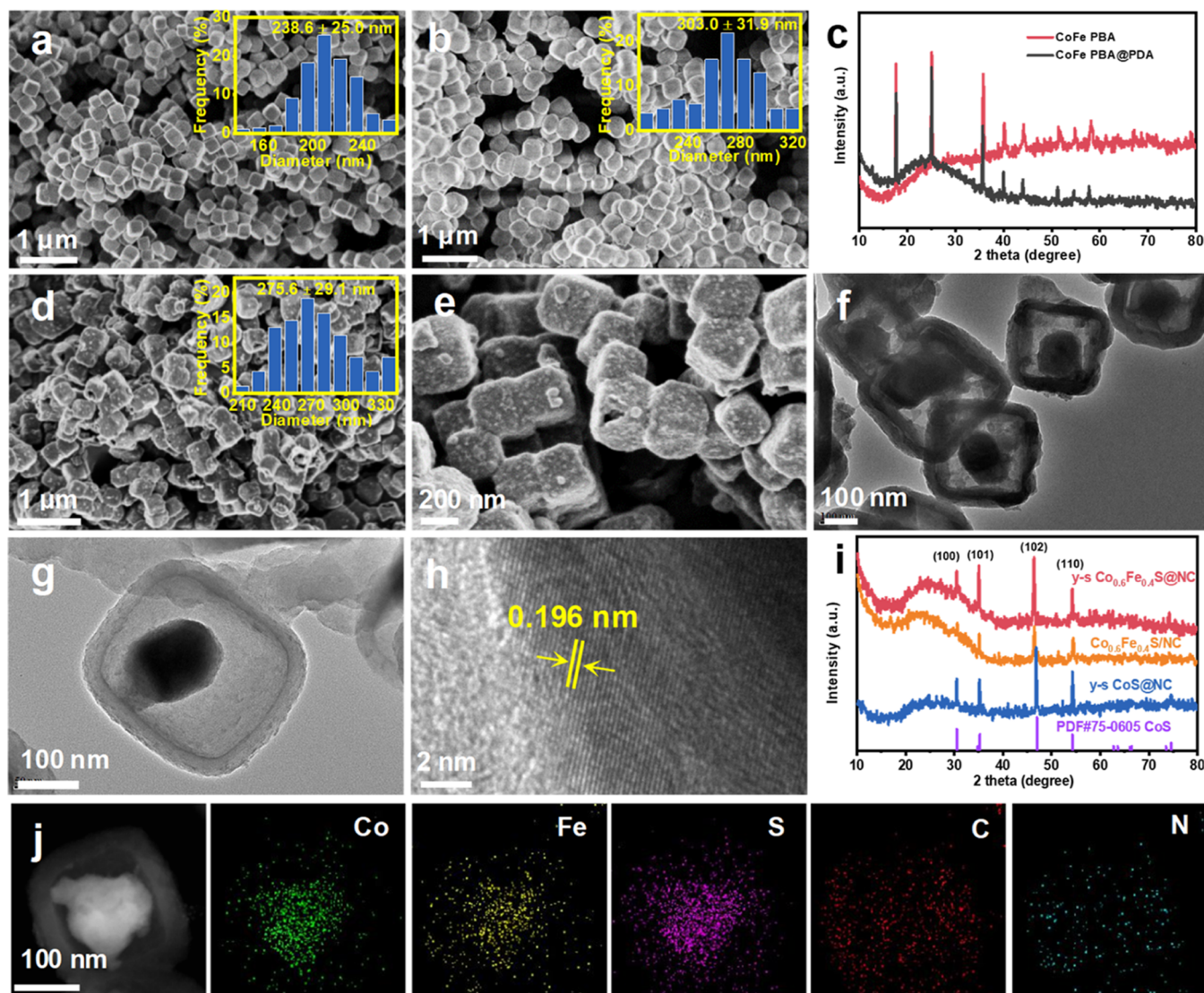


Figure 2. (a,b) SEM images of CoFe PBA and CoFe PBA@PDA, respectively. (c) XRD patterns of CoFe PBA and CoFe PBA@PDA. (d,e) SEM, (f,g) TEM, and (h) HRTEM images of γ -s $\text{Fe}_{0.4}\text{Co}_{0.6}\text{S@NC}$. (i) XRD patterns of γ -s $\text{Fe}_{0.4}\text{Co}_{0.6}\text{S@NC}$, γ -s CoS@NC , and $\text{Fe}_{0.4}\text{Co}_{0.6}\text{S/NC}$. (j) STEM-EDX elemental mapping images for γ -s $\text{Fe}_{0.4}\text{Co}_{0.6}\text{S@NC}$. Inset of (a,b,d): the particle size distribution of CoFe PBA, CoFe PBA@PDA, and γ -s $\text{Fe}_{0.4}\text{Co}_{0.6}\text{S@NC}$, respectively.

patterns of these two compounds (Figure 2c) exhibit the same characteristic diffraction peaks indexed to CoFe PBA (PDF card no. 04-013-49),⁴³ confirming that the PDA covering has virtually no effect on the inner crystal structure of CoFe PBA. Finally, the CoFe PBA@PDA nanocubes were subjected to the sulfidation process at 500 °C for 3 h under Ar, during which the H_2S gas released from the thiourea reacted with them to form γ -s $\text{Fe}_{0.4}\text{Co}_{0.6}\text{S@NC}$ nanocubes. In addition, $\text{Co}_3(\text{Co}(\text{CN})_6)_2 \cdot 2\text{H}_2\text{O}$ (CoCo PBA) and CoCo PBA@PDA were synthesized similarly except for using $\text{Co}[(\text{CN})_6]^{3-}$ as starting anions. Their corresponding SEM images are displayed in Figures S1a and S1b, respectively, demonstrating the formation of solid cubic shapes with a larger size of about 2 μm . Their XRD patterns (Figure S2) correspond well to $\text{Co}_3(\text{Co}(\text{CN})_6)_2 \cdot 12\text{H}_2\text{O}$ (PDF card no. 72-1431). The compared γ -s CoS@NC and $\text{Fe}_{0.4}\text{Co}_{0.6}\text{S/NC}$ were synthesized using CoCo PBA@PDA and CoFe PBA as precursors, respectively.

The SEM images in Figure 2d,e manifest that the γ -s $\text{Fe}_{0.4}\text{Co}_{0.6}\text{S@NC}$ retains its initial cubic shape with an average size of ~ 275.6 nm (inset in Figure 2d) without any structural

destruction after the sulfidation process. The TEM images (Figure 2f,g) display a typical yolk-shell structure with a distinct interior void space. The yolk is $\text{Fe}_{0.4}\text{Co}_{0.6}\text{S}$ nanoparticles with a size of around 100 nm, and the carbon shell thickness is ~ 20 nm. The high-resolution TEM (HRTEM) image (Figure 2h) exhibits an interplanar spacing of 0.196 nm, rising from the (102) planes of CoS [space group $P6_3/mmc$ (194)]. The XRD pattern of γ -s $\text{Fe}_{0.4}\text{Co}_{0.6}\text{S@NC}$ also matches well with the data of the hexagonal CoS phase (PDF card no. 75-0605) given in Figure 2i, confirming the uniform incorporation of Fe ions into CoS by taking the Co-ion sites to form a solid solution phase. Moreover, the (101) and (102) peaks shift to lower angles for γ -s $\text{Fe}_{0.4}\text{Co}_{0.6}\text{S@NC}$ compared to those of γ -s CoS@NC (Figure S3), indicating the expansion of lattice spacing along (101) and (102) directions. Additionally, a broad peak located between 20 and 30° can be observed, which is indexed to amorphous carbon derived from the carbonization of PDA.⁴⁴ Furthermore, the energy-dispersive X-ray spectroscopy (EDX) elemental mapping images reveal that Co, Fe, and S elements are mainly

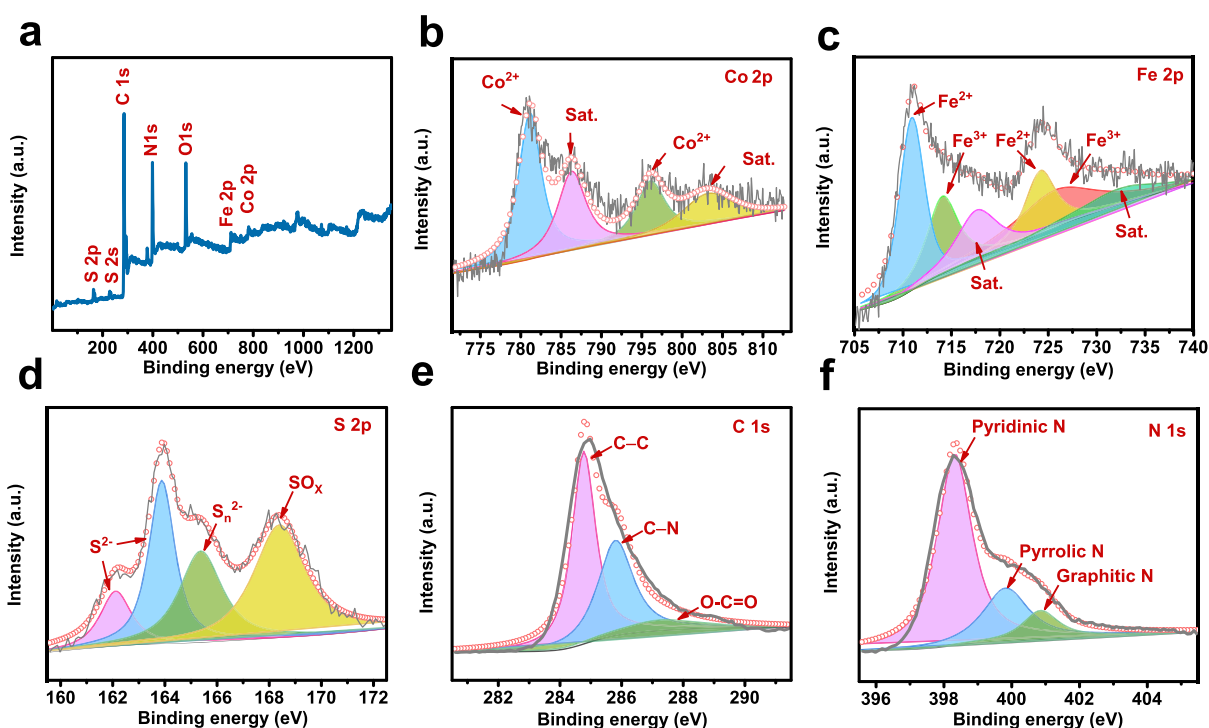


Figure 3. XPS spectra of γ -s $\text{Fe}_{0.4}\text{Co}_{0.6}\text{S@NC}$. (a) Survey, (b) Co 2p, (c) Fe 2p, (d) S 2p, (e) C 1s, and (f) N 1s spectra.

concentrated in the central core and C and N elements are mainly distributed in the cubic shell, verifying the existence of $\text{Fe}_{0.4}\text{Co}_{0.6}\text{S}$ yolk in the N-doped carbon shell (Figure 2j). The concentration of N species is as high as 11.83 at % confirmed by the EDX analysis (Figure S4). The specific surface area of γ -s $\text{Fe}_{0.4}\text{Co}_{0.6}\text{S@NC}$ calculated from the results of BET analysis is $11.47 \text{ m}^2 \text{ g}^{-1}$. Besides, the pore size distribution demonstrates a micro-/mesoporous structure of γ -s $\text{Fe}_{0.4}\text{Co}_{0.6}\text{S@NC}$ with the most probable aperture sizes of 1.89, 2.44, 3.88, and 5.03 nm, as displayed in Figure S5. The yolk-shell structure is significant for the electrochemical behavior of the cathode material. With the advantages of $\text{Fe}_{0.4}\text{Co}_{0.6}\text{S}$ yolk to ensure high capacity, the nitrogen-doped carbon shell to improve the electronic conductivity, the interior void space to accommodate the volume expansion, and micro-/mesopores to facilitate the Al^{3+} diffusion at the electrode/electrolyte interface, satisfactory Al^{3+} storage performance of γ -s $\text{Fe}_{0.4}\text{Co}_{0.6}\text{S@NC}$ can be anticipated. In addition, the ICP results are exhibited in Table S1; the measured average molar ratio of Co and Fe is 1.4:1, consistent with the stoichiometric ratio of their precursors (1.5:1). Interestingly, the compared γ -s CoS@NC possesses the same yolk-shell structure with a larger size of about $2 \mu\text{m}$ (Figure S1c,d). The typical CoS-yolk with N-doped C-shell can be verified by the EDX elemental mapping images, which suggest that Co and S elements are distributed in the central core and C and N elements are located on the cubic shell (Figure S1e). The corresponding XRD pattern further confirms the successful synthesis of the CoS composite (Figure 2i). It is worth noting that the direct sulfidation of the CoFe PBA precursors without the PDA coating would lead to rather different $\text{Fe}_{0.4}\text{Co}_{0.6}\text{S/NC}$ nanoframes composed of heavily aggregated nanoparticles with an average size of 200 nm (Figure S6a,b). Also, their corresponding elemental mapping images display the homogeneous dispersion of Fe, Co, S, C, and N elements within the nanoparticles (Figure S6c). Hence,

the formed carbon acts as an effective buffer, preventing the collapse of the frameworks under a high temperature. In addition, the XRD pattern of this product given in Figure 2i matches well with that of γ -s $\text{Fe}_{0.4}\text{Co}_{0.6}\text{S@NC}$, indicating that the developed facile sulfidation method is effective and general to prepare the Fe-Co-S solid solution using CoFe PBA as the raw material.

XPS was applied to explore the surface chemical states of γ -s $\text{Fe}_{0.4}\text{Co}_{0.6}\text{S@NC}$. The survey spectrum reveals the existence of Fe, Co, S, C, and N elements in the sample (Figure 3a). The deconvolution of the high-resolution XPS (HR-XPS) spectrum of Co 2p displays four peaks (Figure 3b). The peaks at 796.2 and 781.1 eV originate from Co $2p_{1/2}$ and Co $2p_{3/2}$ of Co^{2+} , and the peaks at 786.3 and 803.4 eV correspond to satellite signals, respectively.^{45,46} The HR-XPS Fe 2p spectrum in Figure 3c manifests two different chemical states. Peaks at 711.0 and 724.3 eV are ascribed to Fe^{2+} , and the others at 714.2 and 726.5 eV are related to Fe^{3+} from the surface oxidation layer.⁴⁷ In the HR-XPS S 2p spectrum, four peaks at 162.1, 163.9, 165.4, and 168.4 eV can be observed (Figure 3d). The peaks located at 162.1 and 163.9 eV correspond to sulfide (S^{2-}), whereas the other two peaks at 165.4 and 168.4 eV correspond to S_n^{2-} and oxidized groups (SO_x), respectively.⁴⁸ The C 1s spectrum indicates the presence of C-C (284.8 eV), C-N (285.8 eV), and O-C=O (287.4 eV) bonds (Figure 3e).^{49,50} The presence of the C-N bond verifies that the nitrogen atoms are successfully doped into the carbon matrix via PDA coating layer carbonization, which is also confirmed by the HR-XPS spectrum of N 1s (Figure 3f). The three deconvoluted peaks at 398.3, 399.8, and 400.8 eV reveal the presence of pyridinic-N, pyrrolic-N, and graphite-N, respectively.⁵¹ Additionally, the mass percentage values of the active materials in the γ -s $\text{Fe}_{0.4}\text{Co}_{0.6}\text{S@NC}$, γ -s CoS@NC , and $\text{Fe}_{0.4}\text{Co}_{0.6}\text{S/NC}$ composites are 59.5, 49.3, and 98.6%, respectively, acquired from TGA (Figure S7).

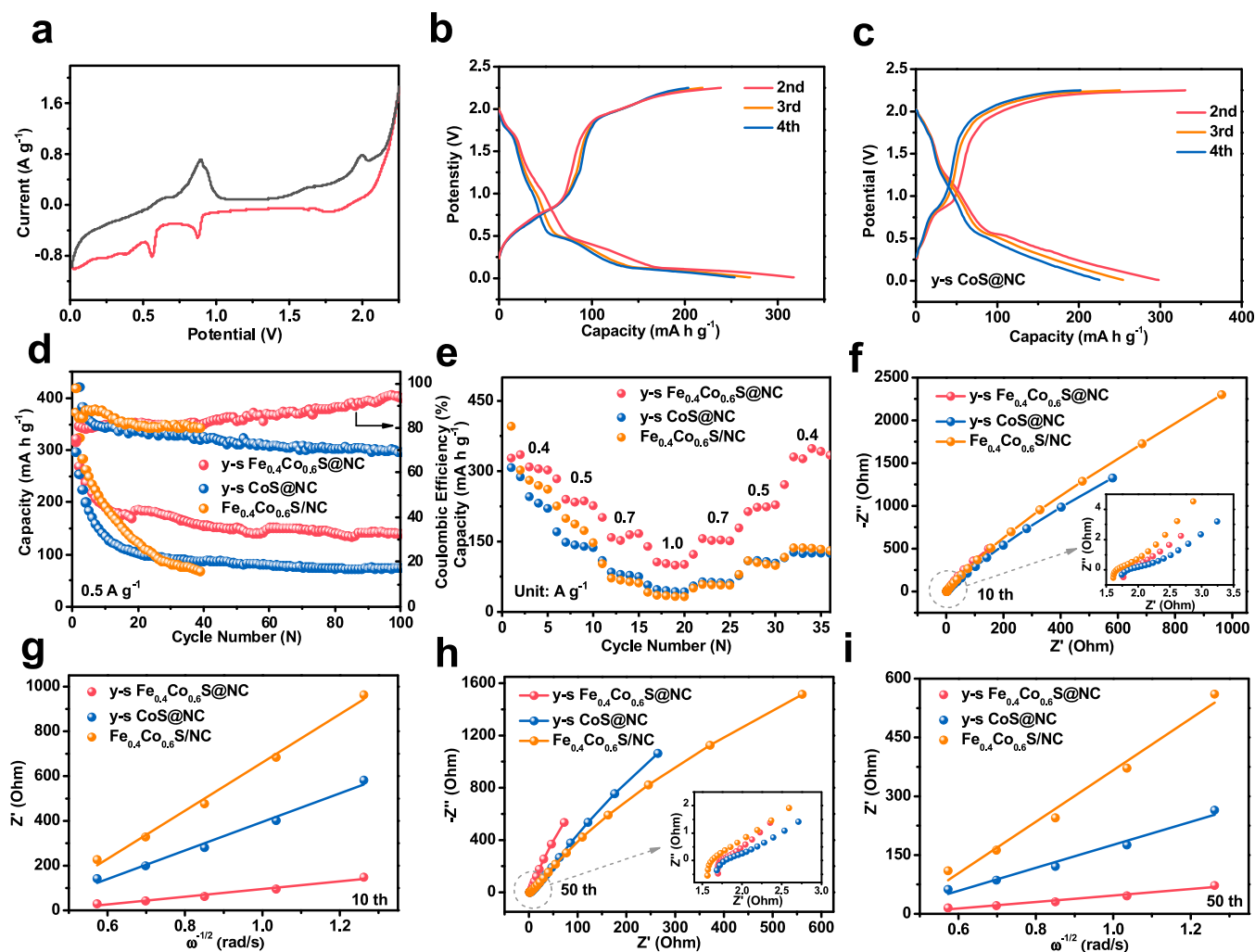


Figure 4. Electrochemical performances of AIB. (a) CV curves of γ -s $\text{Fe}_{0.4}\text{Co}_{0.6}\text{S@NC}$ for the second cycle acquired at 0.5 mV s^{-1} . Selected galvanostatic discharge–charge profiles of (b) γ -s $\text{Fe}_{0.4}\text{Co}_{0.6}\text{S@NC}$ and (c) γ -s CoS@NC at 500 mA g^{-1} . (d) Cycling performance of γ -s $\text{Fe}_{0.4}\text{Co}_{0.6}\text{S@NC}$, γ -s CoS@NC , and $\text{Fe}_{0.4}\text{Co}_{0.6}\text{S/NC}$ at 500 mA g^{-1} . (e) Rate capability of γ -s $\text{Fe}_{0.4}\text{Co}_{0.6}\text{S@NC}$, γ -s CoS@NC , and $\text{Fe}_{0.4}\text{Co}_{0.6}\text{S/NC}$ at various current densities between 400 and 1000 mA g^{-1} . Nyquist impedance plots and relationship between real impedance with low frequency of γ -s $\text{Fe}_{0.4}\text{Co}_{0.6}\text{S@NC}$, γ -s CoS@NC , and $\text{Fe}_{0.4}\text{Co}_{0.6}\text{S/NC}$ [(f,g) after 10 cycles and (h,i) after 50 loops [inset in (f,h) are the magnified Nyquist impedance plots]].

Figure 4 shows the aluminum-ion storage performance of the γ -s $\text{Fe}_{0.4}\text{Co}_{0.6}\text{S@NC}$ electrode investigated by Swagelok-type cells. The CV curves of γ -s $\text{Fe}_{0.4}\text{Co}_{0.6}\text{S@NC}$ in the voltage window of 0.01–2.25 V for the second loop are given in Figure 4a. Three reduction peaks at ca. 0.56, 0.87, and 1.78 V together with the corresponding oxidation peaks at ca. 0.64, 0.89, and 1.99 V can be clearly observed. Notably, the first CV curve of γ -s $\text{Fe}_{0.4}\text{Co}_{0.6}\text{S@NC}$ exhibits a strong peak at 2.13 V (Figure S8), which can be ascribed to side reactions.¹⁸ Compared with the CV curves of γ -s CoS@NC and $\text{Fe}_{0.4}\text{Co}_{0.6}\text{S/NC}$ (Figure S9), that of γ -s $\text{Fe}_{0.4}\text{Co}_{0.6}\text{S@NC}$ displays more distinct peaks corresponding with high electrochemical reaction kinetics. Figures 4b,c and S10 show the selected three-cycle galvanostatic curves of γ -s $\text{Fe}_{0.4}\text{Co}_{0.6}\text{S@NC}$, γ -s CoS@NC , and $\text{Fe}_{0.4}\text{Co}_{0.6}\text{S/NC}$ cathodes at 0.5 A g^{-1} , respectively. All of the observed discharge/charge plateaus of these composites agree well with the peaks in their CV curves. Additionally, the initial charge curve of γ -s $\text{Fe}_{0.4}\text{Co}_{0.6}\text{S@NC}$ given in Figure S11 displays a long and glossy voltage plateau at around 2.06 V, which also coincides well with the initial CV curve.

The cycling performance of these composites at 500 mA g^{-1} is presented in Figure 4d. For γ -s $\text{Fe}_{0.4}\text{Co}_{0.6}\text{S@NC}$, the discharge capacity gradually falls during the first several loops and remains at $191.8 \text{ mA h g}^{-1}$ in the 10th cycle. After 100 cycles, it still gives a reversible capacity of $141.3 \text{ mA h g}^{-1}$, showing good cycling stability. The reasons for the irreversible capacity loss could be either the irreversible solid electrolyte interphase layer formation and the electrolyte decomposition or the active material dissolution and deactivation of reaction sites.^{27,52,53} In addition, for the compared γ -s CoS@NC , the discharge capacity remains only 75.3 mA h g^{-1} in the 100th cycle. Besides, without the N-doped carbon layer covering, the $\text{Fe}_{0.4}\text{Co}_{0.6}\text{S/NC}$ performs inferior cycling behavior. Furthermore, the morphology of γ -s $\text{Fe}_{0.4}\text{Co}_{0.6}\text{S@NC}$ after 100 cycles at 0.5 A g^{-1} was checked by SEM and TEM images (Figure S12a–d). The negligible morphology change of γ -s $\text{Fe}_{0.4}\text{Co}_{0.6}\text{S@NC}$ can be observed, indicating the robust structure of γ -s $\text{Fe}_{0.4}\text{Co}_{0.6}\text{S@NC}$. Meanwhile, the uniform distribution of the elements further confirms the good structural stability of γ -s $\text{Fe}_{0.4}\text{Co}_{0.6}\text{S@NC}$. For comparison, γ -s CoS@NC and $\text{Fe}_{0.4}\text{Co}_{0.6}\text{S/NC}$ exhibit serious structural

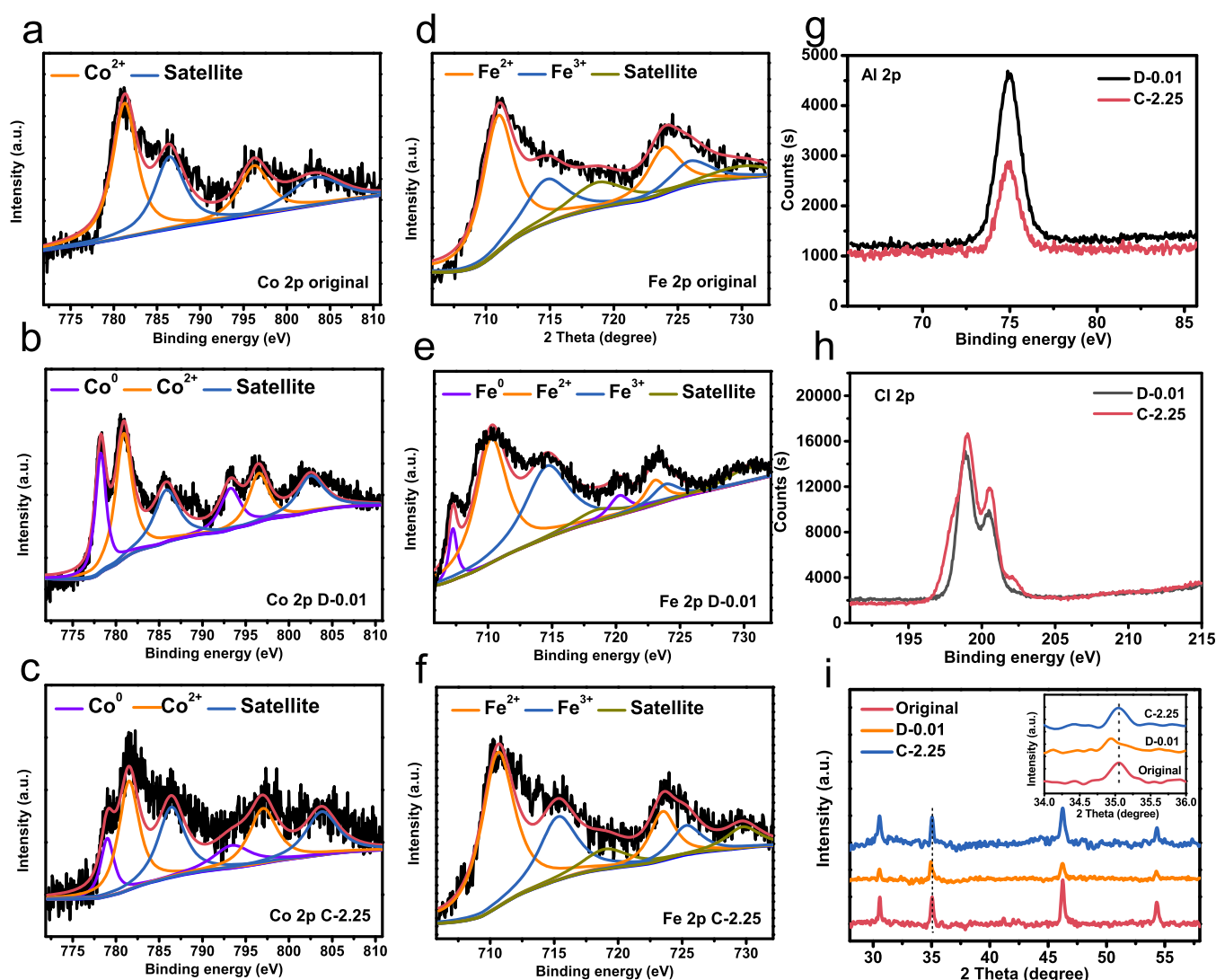


Figure 5. Ex situ XPS results of (a–c) Co 2p, (d–f) Fe 2p, (g) Al 2p, and (h) Cl 2p, and (i) ex situ XRD patterns of $\text{Fe}_{0.4}\text{Co}_{0.6}\text{S}/\text{NC}$ at different reaction states.

damage and aggregation after cycling (Figure S13). Moreover, the electrochemical performance of γ -s $\text{Fe}_{0.4}\text{Co}_{0.6}\text{S}/\text{NC}$ is competitive with or superior to that of the reported metal sulfides (Table S2). The improved cycling performance of γ -s $\text{Fe}_{0.4}\text{Co}_{0.6}\text{S}/\text{NC}$ can be attributed to the following reasons. Fundamentally, the incorporation of Fe into CoS can decrease the Al^{3+} ion diffusion barrier of the cathode. Second, the nitrogen-doped carbon shell can not only further improve the conductivity but also prevent the active $\text{Co}_{0.6}\text{Fe}_{0.4}\text{S}$ particles from aggregation effectively. Moreover, the yolk–shell structure provides an adequate electrolyte penetration area and significantly relieves volume variation.

The rate capability of γ -s $\text{Fe}_{0.4}\text{Co}_{0.6}\text{S}/\text{NC}$, γ -s CoS/NC , and $\text{Fe}_{0.4}\text{Co}_{0.6}\text{S}/\text{NC}$ cathodes was conducted at various rates for every 5 cycles (Figure 4e). The γ -s $\text{Fe}_{0.4}\text{Co}_{0.6}\text{S}/\text{NC}$ displays a high discharge capacity of $302.3 \text{ mA h g}^{-1}$ at 400 mA g^{-1} (for the fifth cycle) and then achieves capacities of 226.2, 166.7, and $100.9 \text{ mA h g}^{-1}$ when the density increases to 500, 700, and 1000 mA g^{-1} , respectively. However, γ -s CoS/NC and $\text{Fe}_{0.4}\text{Co}_{0.6}\text{S}/\text{NC}$ deliver an inferior rate capability, with capacities of 42.8 and 32.3 mA h g^{-1} at 1000 mA g^{-1} , respectively. Impressively, the capacity of γ -s $\text{Fe}_{0.4}\text{Co}_{0.6}\text{S}/\text{NC}$

immediately recovers when the rate returns to 400 mA g^{-1} . The good rate performance confirms the improved reaction kinetics of γ -s $\text{Fe}_{0.4}\text{Co}_{0.6}\text{S}/\text{NC}$, which is due to the Fe incorporation and the advanced yolk–shell structure.

The improved rate performance of γ -s $\text{Fe}_{0.4}\text{Co}_{0.6}\text{S}/\text{NC}$ could be explained via the electrochemical impedance spectroscopy (EIS) conducted on these cathodes after 10 and 50 cycles. As presented in Figure 4f,h, all of the EIS curves show typical Nyquist plots consisting of a high-frequency semicircle followed by an inclined straight line in the low-frequency region, corresponding to the charge transfer resistance (R_{ct}) and Warburg impedance (W), respectively.⁵⁴ After being cycled for 10 and 50 cycles, the γ -s $\text{Fe}_{0.4}\text{Co}_{0.6}\text{S}/\text{NC}$ electrode shows a relatively low charge transfer resistance value, reflecting increased electronic conductivity. Moreover, the diffusion of Al^{3+} can be observed by the slope of the straight line, the larger of which represents faster ion diffusion ability.⁴² More direct results can be obtained from the relationship between frequency and the real part of the impedance converted from the slope line (Figure 4g,i). The smallest slope of γ -s $\text{Fe}_{0.4}\text{Co}_{0.6}\text{S}/\text{NC}$ during the cycling

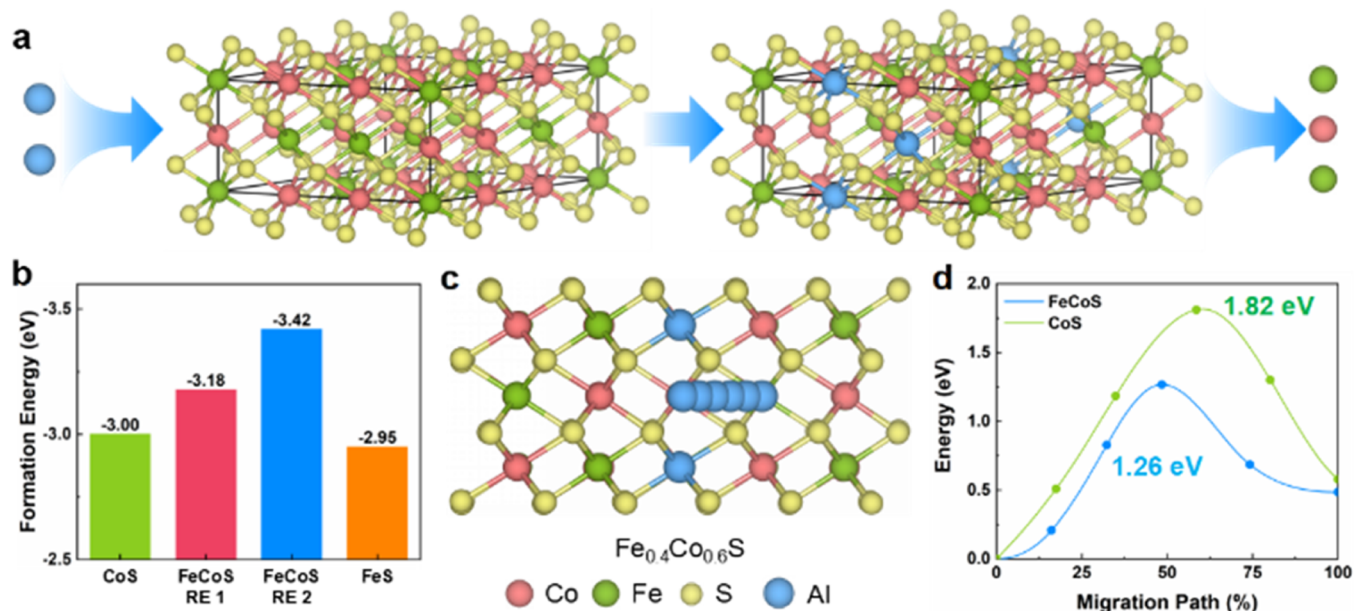


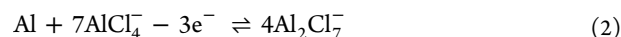
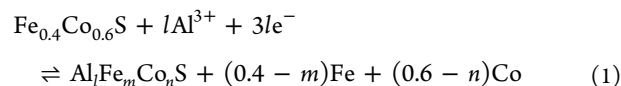
Figure 6. (a) Schematic of the conversion reaction between Al^{3+} and $\text{Fe}_{0.4}\text{Co}_{0.6}\text{S}$. (b) Formation energies of different conversion reactions (RE1 and RE2 are the conversion reactions, where 2Al atoms substitute Fe/Co atoms in $\text{Fe}_{0.4}\text{Co}_{0.6}\text{S}$ with the ratios of 1:2 and 2:1, respectively). (c) Migration path of Al^{3+} in $\text{Fe}_{0.4}\text{Co}_{0.6}\text{S}$. (d) Corresponding energy curves during the Al^{3+} migration process.

process implies faster Al^{3+} diffusion kinetics than γ -s CoS@NC and $\text{Fe}_{0.4}\text{Co}_{0.6}\text{S}/\text{NC}$.⁵⁵

To study the discharge–charge mechanisms of the $\text{Fe}_{0.4}\text{Co}_{0.6}\text{S}$ active material, Swagelok-type cells with $\text{Fe}_{0.4}\text{Co}_{0.6}\text{S}/\text{NC}$ cathodes were disassembled at discharged and charged states after the initial cycle. As shown in Figure 5a–h, XPS spectra of Co 2p, Fe 2p, Al 2p, and Cl 2p at various states are investigated. After fully discharging, new peaks of Co (Co^0 2p_{3/2} at 778.5 eV and Co^0 2p_{1/2} at 793.3 eV) and Fe metal (Fe^0 2p_{3/2} at 707.3 eV and Fe^0 2p_{1/2} at 720.2 eV) appear, which reveal the reduction of $\text{Co}^{2+}/\text{Fe}^{2+}$ to Co^0/Fe^0 , respectively.^{18,56} After recovering to 2.25 V, these peaks belonging to Co^0 and Fe^0 disappear, reflecting that $\text{Fe}_{0.4}\text{Co}_{0.6}\text{S}$ displays great reversible cycling ability and high chemical stability. It is well known that the possible ion storage in the cathode materials of AIBs are Al^{3+} and AlCl_4^- . Due to the opposite charge of these two ions, the intercalation of Al^{3+} and AlCl_4^- needs different initial electrochemical-treated processes.

Specifically, the intercalation of Al^{3+} occurs in the discharging process, while the AlCl_4^- intercalation occurs in the charging process. Therefore, XPS measurements of the cathodes at different states are effective to judge the intercalated ion type. Generally, the AlCl_4^- intercalation often results in higher Al and Cl contents in the charged state than those in the discharged state. Also, the Al^{3+} intercalation often leads to higher Al content in the discharged state than that in the charged state, while the Cl content remains almost the same in these two states. Thus, according to the HR-XPS spectra of Al 2p and Cl 2p displayed in Figure 5g,h, it can be confirmed that the intercalated species in the $\text{Fe}_{0.4}\text{Co}_{0.6}\text{S}$ phase is Al^{3+} rather than AlCl_4^- . Ex situ XRD tests were also performed to further study the structure changes of the $\text{Fe}_{0.4}\text{Co}_{0.6}\text{S}$ phase during the cycling process. A small structure change of $\text{Fe}_{0.4}\text{Co}_{0.6}\text{S}$ occurs during Al^{3+} insertion/de-intercalation processes. As shown in Figure 5i, the peak at 35.0° slightly shifts to lower angle of 34.9° after fully discharging, suggesting a minor enlargement of the interlayer

space corresponding to the (101) plane.^{57,58} Meanwhile, the peak almost shifts to the initial position in the charging process, indicating good stability of the $\text{Fe}_{0.4}\text{Co}_{0.6}\text{S}$ phase.⁵⁷ Based on the above analysis, the possible reaction during the electrochemical process can be described as in eqs 1 and 2, for cathode and anode, respectively.



In the $\text{Fe}_{0.4}\text{Co}_{0.6}\text{S}$ cathode, Al^{3+} ions originated from complex Al_2Cl_7^- anion decomposition intercalate into the $\text{Fe}_{0.4}\text{Co}_{0.6}\text{S}$ material during discharging to form $\text{Al}_l\text{Fe}_m\text{Co}_n\text{S}$ and elemental Fe and Co, which is similar to our previous report for the $\text{Ni}_{0.6}\text{Co}_{0.4}\text{S}$ cathode.³⁰ The reverse reaction takes place during the charging process. Concurrently, the aluminum shedding and deposition reactions take place in the Al anode.

To further interpret the improved aluminum storage performance of the $\text{Fe}_{0.4}\text{Co}_{0.6}\text{S}$ solid solution, a theoretical Al^{3+} storage ability of $\text{Fe}_{0.4}\text{Co}_{0.6}\text{S}$ was calculated via DFT. The thermodynamic calculations of the electrochemical reactions between Al^{3+} and CoS, FeS, and $\text{Fe}_{0.4}\text{Co}_{0.6}\text{S}$ were conducted first. According to the mechanism of conversion reaction, the reaction process can be simulated via substituting three Co/Fe atoms with two Al atoms in the sulfide crystals. Specifically, the pristine sulfide CoS/FeS phases are partially substituted with the Al, resulting in the formation of Co/Fe atoms, in which the molar ratio of Al/Co and Al/Fe is the same (2:3). However, the reaction between two Al^{3+} and FeCoS involves two different reaction types, leading to the generation of Fe/Co atoms with a ratio of 1:2 (defined as reaction 1) and 2:1 (defined as reaction 2). Figure 6a schematically displays the reaction process of reaction 2, and the thermodynamic formation energies of these reactions are summarized in Figure 6b. Obviously, the formation energies of the conversion reactions between Al^{3+} and solid solution phase $\text{Fe}_{0.4}\text{Co}_{0.6}\text{S}$ are

more negative, meaning that the solid solution can promote the electrochemical reaction, improve the reaction degree, and enhance the utilization rate of the electrode material. The diffusion process of Al^{3+} in CoS and $\text{Fe}_{0.4}\text{Co}_{0.6}\text{S}$ was simulated using the CI-NEB method. The possible Al^{3+} migration paths in $\text{Fe}_{0.4}\text{Co}_{0.6}\text{S}$ and CoS are given in Figures 6c and S14, respectively. Figure 6d shows their corresponding energy curves during the Al^{3+} migration process. It can be observed that the formation of solid solution reduces the Al^{3+} diffusion energy barrier from 1.82 to 1.26 eV, indicating that the introduction of Fe can facilitate the Al^{3+} diffusion and promote the electrochemical performance.

4. CONCLUSIONS

In summary, according to electrochemical experiments and DFT calculations, we demonstrate that the clumsy Al^{3+} diffusion kinetics can be effectively improved by dissolution of Fe^{2+} into the CoS to form the $\text{Fe}_{0.4}\text{Co}_{0.6}\text{S}$ solid solution. Fe^{2+} introduced into the CoS lattice will lead to more negative Al^{3+} formation energy and lower Al^{3+} ions diffusion barrier, contributing to enhanced cycling capacity and rate capability. The cycling stability is guaranteed mainly by the interior void space and the external carbon shell, of which the former can relieve volume variation and the later can enhance electronic conductivity and inhibit $\text{Fe}_{0.4}\text{Co}_{0.6}\text{S}$ from self-aggregate during cycling test. As a result, the designed γ -s $\text{Fe}_{0.4}\text{Co}_{0.6}\text{S}@NC$ cathode delivers high capacity, good rate capability, and ideal cycling stability. Furthermore, investigation of the γ -s $\text{Fe}_{0.4}\text{Co}_{0.6}\text{S}@NC$ aluminum storage mechanism discloses the intercalation of Al^{3+} into $\text{Fe}_{0.4}\text{Co}_{0.6}\text{S}$ to generate $\text{AlFe}_m\text{Co}_n\text{S}$ and elemental Fe and Co. This work can provide a new avenue to enhance the aluminum storage performance of the sulfide cathode materials.

■ ASSOCIATED CONTENT

SI Supporting Information

The Supporting Information is available free of charge at <https://pubs.acs.org/doi/10.1021/acsami.1c24510>.

Additional SEM, TEM, EDX, XRD, BET, and TGA; additional electrochemical performance of γ -s $\text{Fe}_{0.4}\text{Co}_{0.6}\text{S}@NC$, γ -s CoS@NC, and $\text{Fe}_{0.4}\text{Co}_{0.6}\text{S}/NC$ at initial discharge-charge cycles; morphology measurements of cathode materials after 100 cycles; migration path of Al^{3+} in CoS; table of element composition of γ -s $\text{Fe}_{0.4}\text{Co}_{0.6}\text{S}@NC$; table of electrochemical performance comparison; and additional references (PDF)

■ AUTHOR INFORMATION

Corresponding Author

Xuebin Yu – Department of Materials Science, Fudan University, Shanghai 200433, China; orcid.org/0000-0002-4035-0991; Email: yuxuebin@fudan.edu.cn

Authors

Jiening Zheng – Department of Materials Science, Fudan University, Shanghai 200433, China

Shunlong Ju – Department of Materials Science, Fudan University, Shanghai 200433, China

Guanglin Xia – Department of Materials Science, Fudan University, Shanghai 200433, China; orcid.org/0000-0002-3493-4309

Hongge Pan – Institute of Science and Technology for New Energy, Xi'an Technological University, Xi'an 710021, China

Complete contact information is available at: <https://pubs.acs.org/doi/10.1021/acsami.1c24510>

Author Contributions

§J.Z. and S.J. contributed equally to this work.

Notes

The authors declare no competing financial interest.

■ ACKNOWLEDGMENTS

This work was partially supported by the National Key Research and Development Program of China (2017YFA0204600), the National Science Fund for Distinguished Young Scholars (51625102), the National Natural Science Foundation of China (51971065), and the Innovation Program of Shanghai Municipal Education Commission (2019-01-07-00-07-E00028).

■ REFERENCES

- (1) Kang, K.; Meng, Y. S.; Bréger, J.; Grey, C. P.; Ceder, G. Electrodes with High Power and High Capacity for Rechargeable Lithium Batteries. *Science* **2006**, *311*, 977–980.
- (2) Magasinski, A.; Dixon, P.; Hertzberg, B.; Kvit, A.; Ayala, J.; Yushin, G. High-Performance Lithium-Ion Anodes Using a Hierarchical Bottom-Up Approach. *Nat. Mater.* **2010**, *9*, 353–358.
- (3) Dunn, B.; Kamath, H.; Tarascon, J.-M. Electrical Energy Storage for the Grid: A Battery of Choices. *Science* **2011**, *334*, 928–935.
- (4) Choi, J. W.; Aurbach, D. Promise and reality of post-lithium-ion batteries with high energy densities. *Nat. Rev. Mater.* **2016**, *1*, 16013.
- (5) Shen, X.; Zhou, Q.; Han, M.; Qi, X.; Li, B.; Zhang, Q.; Zhao, J.; Yang, C.; Liu, H.; Hu, Y.-S. Rapid Mechanochemical Synthesis of Polyanionic Cathode with Improved Electrochemical Performance for Na-Ion Batteries. *Nat. Commun.* **2021**, *12*, 2848.
- (6) Zhang, W.; Liu, Y.; Guo, Z. Approaching High-Performance Potassium-Ion Batteries via Advanced Design Strategies and Engineering. *Sci. Adv.* **2019**, *5*, No. eaav7412.
- (7) Zhang, W.; Lu, J.; Guo, Z. Challenges and Future Perspectives on Sodium and Potassium Ion Batteries for Grid-Scale Energy Storage. *Mater. Today* **2021**, *50*, 400–417.
- (8) Liang, Y.; Dong, H.; Aurbach, D.; Yao, Y. Current Status and Future Directions of Multivalent Metal-Ion Batteries. *Nat. Energy* **2020**, *5*, 646–656.
- (9) Koketsu, T.; Ma, J.; Morgan, B. J.; Body, M.; Legein, C.; Dachraoui, W.; Giannini, M.; Demortière, A.; Salanne, M.; Dardoize, F.; Groult, H.; Borkiewicz, O. J.; Chapman, K. W.; Strasser, P.; Dambournet, D. Reversible Magnesium and Aluminium Ions Insertion in Cation-Deficient Anatase TiO_2 . *Nat. Mater.* **2017**, *16*, 1142–1148.
- (10) Zeng, X.; Xie, K.; Liu, S.; Zhang, S.; Hao, J.; Liu, J.; Pang, W. K.; Liu, J.; Rao, P.; Wang, Q.; Mao, J.; Guo, Z. Bio-Inspired Design of an In Situ Multifunctional Polymeric Solid-Electrolyte Interphase for Zn Metal Anode Cycling at 30 mA cm^{-2} and 30 mA h cm^{-2} . *Energy Environ. Sci.* **2021**, *14*, 5947–5957.
- (11) Liu, S.; Mao, J.; Pang, W. K.; Vongsvivut, J.; Zeng, X.; Thomsen, L.; Wang, Y.; Liu, J.; Li, D.; Guo, Z. Tuning the Electrolyte Solvation Structure to Suppress Cathode Dissolution, Water Reactivity, and Zn Dendrite Growth in Zinc-Ion Batteries. *Adv. Funct. Mater.* **2021**, *31*, 2104281.
- (12) Elia, G. A.; Marquardt, K.; Hoepfner, K.; Fantini, S.; Lin, R.; Knipping, E.; Peters, W.; Drillet, J.-F.; Passerini, S.; Hahn, R. An Overview and Future Perspectives of Aluminum Batteries. *Nat. Commun.* **2016**, *28*, 7564–7579.
- (13) Zhang, Y.; Liu, S.; Ji, Y.; Ma, J.; Yu, H. Emerging Nonaqueous Aluminum-Ion Batteries: Challenges, Status, and Perspectives. *Adv. Mater.* **2018**, *30*, 1706310.

- (14) Lin, M.-C.; Gong, M.; Lu, B.; Wu, Y.; Wang, D.-Y.; Guan, M.; Angell, M.; Chen, C.; Yang, J.; Hwang, B.-J.; Dai, H. An Ultrafast Rechargeable Aluminium-Ion Battery. *Nature* **2015**, *520*, 324–328.
- (15) Wang, D.-Y.; Wei, C.-Y.; Lin, M.-C.; Pan, C.-J.; Chou, H.-L.; Chen, H.-A.; Gong, M.; Wu, Y.; Yuan, C.; Angell, M.; Hsieh, Y.-J.; Chen, Y.-H.; Wen, C.-Y.; Chen, C.-W.; Hwang, B.-J.; Chen, C.-C.; Dai, H. Advanced Rechargeable Aluminium Ion Battery with a High-Quality Natural Graphite Cathode. *Nat. Commun.* **2017**, *8*, 14283.
- (16) Hu, Y.; Ye, D.; Luo, B.; Hu, H.; Zhu, X.; Wang, S.; Li, L.; Peng, S.; Wang, L. A Binder-Free and Free-Standing Cobalt Sulfide@Carbon Nanotube Cathode Material for Aluminium-Ion Batteries. *Adv. Mater.* **2018**, *30*, 1703824.
- (17) Yang, H.; Li, H.; Li, J.; Sun, Z.; He, K.; Cheng, H. M.; Li, F. The Rechargeable Aluminum Battery: Opportunities and Challenges. *Angew. Chem., Int. Ed.* **2019**, *58*, 11978–11996.
- (18) Cai, T.; Zhao, L.; Hu, H.; Li, T.; Li, X.; Guo, S.; Li, Y.; Xue, Q.; Xing, W.; Yan, Z.; Wang, L. Stable CoSe₂/Carbon Nanodice@Reduced Graphene Oxide Composites for High-Performance Rechargeable Aluminum-Ion Batteries. *Energy Environ. Sci.* **2018**, *11*, 2341–2347.
- (19) Lu, H.; Wan, Y.; Wang, T.; Jin, R.; Ding, P.; Wang, R.; Wang, Y.; Teng, C.; Li, L.; Wang, X.; Zhou, D.; Xue, G. A High Performance SnO₂/C Nanocomposite Cathode for Aluminum-Ion Batteries. *J. Mater. Chem. A* **2019**, *7*, 7213–7220.
- (20) Lu, S.; Wang, M.; Guo, F.; Tu, J.; Lv, A.; Chen, Y.; Jiao, S. Self-Supporting and High-Loading Hierarchically Porous Co-P Cathode for Advanced Al-Ion Battery. *Chem. Eng. J.* **2020**, *389*, 124370.
- (21) Ai, Y.; Wu, S.-C.; Wang, K.; Yang, T.-Y.; Liu, M.; Liao, H.-J.; Sun, J.; Chen, J.-H.; Tang, S.-Y.; Wu, D. C.; Su, T.-Y.; Wang, Y.-C.; Chen, H.-C.; Zhang, S.; Liu, W.-W.; Chen, Y.-Z.; Lee, L.; He, J.-H.; Wang, Z. M.; Chueh, Y.-L. Three-Dimensional Molybdenum Diselenide Helical Nanorod Arrays for High-Performance Aluminium-Ion Batteries. *ACS Nano* **2020**, *14*, 8539–8550.
- (22) VahidMohammadi, A.; Hadjikhani, A.; Shahbazmohamadi, S.; Beidaghi, M. Two-Dimensional Vanadium Carbide (MXene) as a High-Capacity Cathode Material for Rechargeable Aluminum Batteries. *ACS Nano* **2017**, *11*, 11135–11144.
- (23) Yao, L.; Ju, S.; Xu, T.; Yu, X. Spatial Isolation-Inspired Ultrafine CoSe₂ for High-Energy Aluminum Batteries with Improved Rate Cyclability. *ACS Nano* **2021**, *15*, 13662–13673.
- (24) Du, Y.; Zhang, B.; Zhang, W.; Jin, H.; Qin, J.; Wan, J.; Zhang, J.; Chen, G. Interfacial Engineering of Bi₂Te₃/Sb₂Te₃ Heterojunction Enables High-Energy Cathode for Aluminum Batteries. *Energy Storage Mater.* **2021**, *38*, 231–240.
- (25) Li, H.; Yang, H.; Sun, Z.; Shi, Y.; Cheng, H.-M.; Li, F. A Highly Reversible Co₃S₄ Microsphere Cathode Material for Aluminum-Ion Batteries. *Nano Energy* **2019**, *56*, 100–108.
- (26) Tu, J.; Xiao, X.; Wang, M.; Jiao, S. Hierarchical Flower-Like MoS₂ Microspheres and Their Efficient Al Storage Properties. *J. Phys. Chem. C* **2019**, *123*, 26794–26802.
- (27) Wang, S.; Jiao, S.; Wang, J.; Chen, H.-S.; Tian, D.; Lei, H.; Fang, D.-N. High-Performance Aluminum-Ion Battery with CuS@C Microsphere Composite Cathode. *ACS Nano* **2017**, *11*, 469–477.
- (28) Xing, W.; Du, D.; Cai, T.; Li, X.; Zhou, J.; Chai, Y.; Xue, Q.; Yan, Z. Carbon-Encapsulated CoSe Nanoparticles Derived from Metal-Organic Frameworks as Advanced Cathode Material for Al-ion battery. *J. Power Sources* **2018**, *401*, 6–12.
- (29) Jadhav, A. L.; Xu, J. H.; Messinger, R. J. Quantitative Molecular-Level Understanding of Electrochemical Aluminum-Ion Intercalation into a Crystalline Battery Electrode. *ACS Energy Lett.* **2020**, *5*, 2842–2848.
- (30) Zheng, J.; Ju, S.; Yao, L.; Xia, G.; Yu, X. Construction of Solid Solution Sulfide Embedded in MXene@N-doped Carbon Dual Protection Matrix for Advanced Aluminum Ion Batteries. *J. Power Sources* **2021**, *511*, 230450.
- (31) Barik, G.; Pal, S. Monolayer Transition-Metal Dichalcogenide Mo_{1-x}W_xS₂ Alloys as Efficient Anode Materials for Lithium-Ion Batteries. *J. Phys. Chem. C* **2018**, *122*, 25837–25848.
- (32) Zhang, D.; Cao, J.; Zhang, X.; Insin, N.; Wang, S.; Han, J.; Zhao, Y.; Qin, J.; Huang, Y. Inhibition of Manganese Dissolution in Mn₂O₃ Cathode with Controllable Ni²⁺ Incorporation for High-Performance Zinc Ion Battery. *Adv. Funct. Mater.* **2021**, *31*, 2009412.
- (33) Wang, J.; Zhang, L.; Sun, K.; He, J.; Zheng, Y.; Xu, C.; Zhang, Y.; Chen, Y.; Li, M. Improving Ionic/Electronic Conductivity of MoS₂ Li-ion Anode Via Manganese Doping and Structural Optimization. *Chem. Eng. J.* **2019**, *372*, 665–672.
- (34) Yu, L.; Guan, B.; Xiao, W.; Lou, X. W. D. Formation of Yolk-Shelled Ni-Co Mixed Oxide Nanoprisms with Enhanced Electrochemical Performance for Hybrid Supercapacitors and Lithium Ion Batteries. *Adv. Energy Mater.* **2015**, *5*, 1500981.
- (35) Wu, C.; Tong, X.; Ai, Y.; Liu, D.-S.; Yu, P.; Wu, J.; Wang, Z. M. A Review: Enhanced Anodes of Li/Na-Ion Batteries Based on Yolk-Shell Structured Nanomaterials. *Nano-Micro Lett.* **2018**, *10*, 40.
- (36) Wang, Y.-X.; Yang, J.; Chou, S.-L.; Liu, H. K.; Zhang, W.-x.; Zhao, D.; Dou, S. X. Uniform yolk-shell iron sulfide-carbon nanospheres for superior sodium-iron sulfide batteries. *Nat. Commun.* **2015**, *6*, 8689.
- (37) Zhao, Y.; Zhu, J.; Ong, S. J. H.; Yao, Q.; Shi, X.; Hou, K.; Xu, Z. J.; Guan, L. High-Rate and Ultralong Cycle-Life Potassium Ion Batteries Enabled by In Situ Engineering of Yolk-Shell FeS₂@C Structure on Graphene Matrix. *Adv. Energy Mater.* **2018**, *8*, 1802565.
- (38) Zhang, Z.; Du, Y.; Wang, Q. C.; Xu, J.; Zhou, Y. N.; Bao, J.; Shen, J.; Zhou, X. A Yolk-Shell-Structured FePO₄ Cathode for High-Rate and Long-Cycling Sodium-Ion Batteries. *Angew. Chem., Int. Ed.* **2020**, *59*, 17504–17510.
- (39) Li, W.; Ma, Q.; Shen, P.; Zhou, Y.; Soule, L.; Li, Y.; Wu, Y.; Zhang, H.; Liu, M. Yolk-Shell Structured CuSi₂P₃@Graphene Nanocomposite Anode for Long-Life and High-Rate Lithium-Ion Batteries. *Nano Energy* **2021**, *80*, 105506.
- (40) Wang, J.; Zhu, L.; Li, F.; Yao, T.; Liu, T.; Cheng, Y.; Yin, Z.; Wang, H. Synergizing Phase and Cavity in CoMoO_xS_y Yolk-Shell Anodes to Co-Enhance Capacity and Rate Capability in Sodium Storage. *Small* **2020**, *16*, 2002487.
- (41) Chu, J.; Yu, Q.; Han, K.; Xing, L.; Gu, C.; Li, Y.; Bao, Y.; Wang, W. Yolk-Shell Structured FeS/MoS₂@Nitrogen-Doped Carbon Nanocubes with Sufficient Internal Void Space as an Ultrastable Anode for Potassium-Ion Batteries. *J. Mater. Chem. A* **2020**, *8*, 23983–23993.
- (42) Liu, W.; Ju, S.; Yu, X. Phosphorus-Amine-Based Synthesis of Nanoscale Red Phosphorus for Application to Sodium-Ion Batteries. *ACS Nano* **2020**, *14*, 974–984.
- (43) Chen, Y.; Zhang, W.; Zhou, D.; Tian, H.; Su, D.; Wang, C.; Stockdale, D.; Kang, F.; Li, B.; Wang, G. Co-Fe Mixed Metal Phosphide Nanocubes with Highly Interconnected-Pore Architecture as an Efficient Polysulfide Mediator for Lithium-Sulfur Batteries. *ACS Nano* **2019**, *13*, 4731–4741.
- (44) Zou, Y.; Gu, Y.; Hui, B.; Yang, X.; Liu, H.; Chen, S.; Cai, R.; Sun, J.; Zhang, X.; Yang, D. Nitrogen and Sulfur Vacancies in Carbon Shell to Tune Charge Distribution of Co₆Ni₃S₈ Core and Boost Sodium Storage. *Adv. Energy Mater.* **2020**, *10*, 1904147.
- (45) Yousaf, M.; Chen, Y.; Tabassum, H.; Wang, Z.; Wang, Y.; Abid, A. Y.; Mahmood, A.; Mahmood, N.; Guo, S.; Han, R. P. S.; Gao, P. A Dual Protection System for Heterostructured 3D CNT/CoSe₂/C as High Areal Capacity Anode for Sodium Storage. *Adv. Sci.* **2020**, *7*, 1902907.
- (46) Chen, J.; Pan, A.; Wang, Y.; Cao, X.; Zhang, W.; Kong, X.; Su, Q.; Lin, J.; Cao, G.; Liang, S. Hierarchical Mesoporous MoSe₂@CoSe/N-Doped Carbon Nanocomposite for Sodium Ion Batteries and Hydrogen Evolution Reaction Applications. *Energy Storage Mater.* **2019**, *21*, 97–106.
- (47) Xiao, Y.; Hwang, J.-Y.; Belharouak, I.; Sun, Y.-K. Na Storage Capability Investigation of a Carbon Nanotube-Encapsulated Fe_{1-x}S Composite. *ACS Energy Lett.* **2017**, *2*, 364–372.
- (48) Cao, D.; Kang, W.; Wang, S.; Wang, Y.; Sun, K.; Yang, L.; Zhou, X.; Sun, D.; Cao, Y. In situ N-Doped Carbon Modified (Co_{0.5}Ni_{0.5})₂S₈ Solid-Solution Hollow Spheres as High-Capacity

Anodes for Sodium-Ion Batteries. *J. Mater. Chem. A* **2019**, *7*, 8268–8276.

(49) Tian, J.; Li, J.; Zhang, Y.; Yu, X.-Y.; Hong, Z. Carbon-Coated CoSe₂ Nanoparticles Confined in N-Doped Carbon Microboxes with Enhanced Sodium Storage Properties. *J. Mater. Chem. A* **2019**, *7*, 21404–21409.

(50) Cao, L.; Gao, X.; Zhang, B.; Ou, X.; Zhang, J.; Luo, W.-B. Bimetallic Sulfide Sb₂S₃@FeS₂ Hollow Nanorods as High-Performance Anode Materials for Sodium-Ion Batteries. *ACS Nano* **2020**, *14*, 3610–3620.

(51) Lin, Y.; Qiu, Z.; Li, D.; Ullah, S.; Hai, Y.; Xin, H.; Liao, W.; Yang, B.; Fan, H.; Xu, J.; Zhu, C. NiS₂@CoS₂ Nanocrystals Encapsulated in N-doped Carbon Nanocubes for High Performance Lithium/Sodium Ion Batteries. *Energy Storage Mater.* **2018**, *11*, 67–74.

(52) Hu, Y.; Luo, B.; Ye, D.; Zhu, X.; Lyu, M.; Wang, L. An Innovative Freeze-Dried Reduced Graphene Oxide Supported SnS₂ Cathode Active Material for Aluminum-Ion Batteries. *Adv. Mater.* **2017**, *29*, 1606132.

(53) Liu, S.; Mao, J.; Zhang, L.; Pang, W. K.; Du, A.; Guo, Z. Manipulating the Solvation Structure of Nonflammable Electrolyte and Interface to Enable Unprecedented Stability of Graphite Anodes beyond 2 Years for Safe Potassium-Ion Batteries. *Adv. Mater.* **2021**, *33*, 2006313.

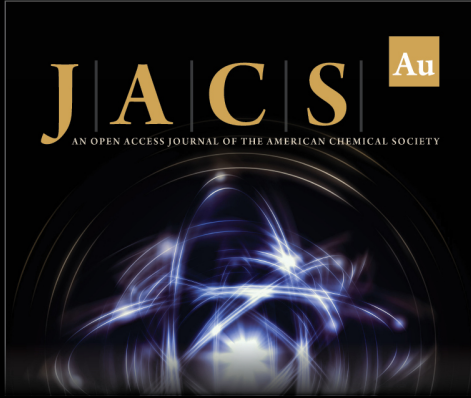
(54) Xu, X.; Zhang, Y.; Sun, H.; Zhou, J.; Liu, Z.; Qiu, Z.; Wang, D.; Yang, C.; Zeng, Q.; Peng, Z.; Guo, S. Orthorhombic Cobalt Ditetelluride with Te Vacancy Defects Anchoring on Elastic MXene Enables Efficient Potassium-Ion Storage. *Adv. Mater.* **2021**, *33*, 2100272.

(55) Wang, B.; Yan, J.; Zhang, Y.; Ye, M.; Yang, Y.; Li, C. C. In Situ Carbon Insertion in Laminated Molybdenum Dioxide by Interlayer Engineering Toward Ultrastable “Rocking-Chair” Zinc-Ion Batteries. *Adv. Funct. Mater.* **2021**, *31*, 2102827.

(56) Ali-Löytty, H.; Louie, M. W.; Singh, M. R.; Li, L.; Sanchez Casalongue, H. G.; Ogasawara, H.; Crumlin, E. J.; Liu, Z.; Bell, A. T.; Nilsson, A.; Friebel, D. Ambient-Pressure XPS Study of a Ni–Fe Electrocatalyst for the Oxygen Evolution Reaction. *J. Phys. Chem. C* **2016**, *120*, 2247–2253.


(57) Wu, L.; Sun, R.; Xiong, F.; Pei, C.; Han, K.; Peng, C.; Fan, Y.; Yang, W.; An, Q.; Mai, L. A Rechargeable Aluminum-Ion Battery Based on a VS₂ Nanosheet Cathode. *Phys. Chem. Chem. Phys.* **2018**, *20*, 22563–22568.


(58) Xing, L.; Owusu, K. A.; Liu, X.; Meng, J.; Wang, K.; An, Q.; Mai, L. Insights Into the Storage Mechanism of VS₄ Nanowire Clusters in Aluminum-Ion Battery. *Nano Energy* **2021**, *79*, 105384.



JACS Au
AN OPEN ACCESS JOURNAL OF THE AMERICAN CHEMICAL SOCIETY

Editor-in-Chief
Prof. Christopher W. Jones
Georgia Institute of Technology, USA

Open for Submissions 

pubs.acs.org/jacsau  ACS Publications
Most Trusted. Most Cited. Most Read.